photonics

MDPI

Article

Theoretical Investigation of Terahertz Spoof Surface-Plasmon-Polariton Devices Based on Ring Resonators

Can Liu [1], Shenghao Gu [1], Mingming Sun [1], Ya Liu [1], Ying Zhang [1,*] and Jiaguang Han [2,3]

[1] Yunnan Key Laboratory of Opto-Electronic Information Technology and Institute of Physics and Electronic Information, Yunnan Normal University, Kunming 650500, China; 2223090031@ynnu.edu.cn (C.L.); liuya@ynnu.edu.cn (Y.L.)
[2] Guangxi Key Laboratory of Optoelectronic Information Processing, School of Optoelectronic Engineering, Guilin University of Electronic Technology, Guilin 541004, China; jiaghan@tju.edu.cn
[3] Center for Terahertz Waves and College of Precision Instrument and Optoelectronics Engineering, Tianjin University, and Key Laboratory of Optoelectronics Information and Technology, Ministry of Education of China, Tianjin 300072, China
* Correspondence: yingzhang27@ynnu.edu.cn

Abstract: Terahertz is one of the most promising technologies for high-speed communication and large-scale data transmission. As a classical optical component, ring resonators are extensively utilized in the design of band-pass and frequency-selective devices across various wavebands, owing to their unique characteristics, including optical comb generation, compactness, and low manufacturing cost. While substantial progress has been made in the study of ring resonators, their application in terahertz surface wave systems remains less than fully optimized. This paper presents several spoof surface plasmon polariton-based devices, which were realized using ring resonators at terahertz frequencies. The influence of both the radius of the ring resonator and the width of the waveguide coupling gap on the coupling coefficient are investigated. The band-stop filters based on the cascaded ring resonator exhibit a 0.005 THz broader frequency bandwidth compared to the single-ring resonator filter and achieve a minimum stopband attenuation of 28 dB. The add–drop multiplexers based on the asymmetric ring resonator enable selective surface wave outputs at different ports by rotating the ring resonator. The devices designed in this study offer valuable insights for the development of on-chip terahertz components.

Keywords: spoof surface plasmon polaritons; ring resonator; terahertz wave; functional devices

check for updates

Received: 9 December 2024
Revised: 5 January 2025
Accepted: 8 January 2025
Published: 15 January 2025

Citation: Liu, C.; Gu, S.; Sun, M.; Liu, Y.; Zhang, Y.; Han, J. Theoretical Investigation of Terahertz Spoof Surface-Plasmon-Polariton Devices Based on Ring Resonators. *Photonics* **2025**, *12*, 70. https://doi.org/10.3390/photonics12010070

1. Introduction

Terahertz waves exhibit unique characteristics such as low photon energy, good penetrability, and excellent capability for spectral analysis [1,2]. These attributes render THz technology highly versatile across various fields, including high-speed communication, non-destructive inspection, security checks, biology research, cancer diagnosis, and so on [3–7]. However, existing optical devices are often bulky and lossy, which limit their applicability in advanced technologies. On the other hand, on-chip or integrated optical devices whose dimensions are significantly smaller than their free-space counterparts have attracted considerable interest. Surface Plasmon Polaritons (SPPs) have become one of the most promising technologies for developing an optical on-chip integrated system. This is mainly attributed to their excellent binding ability and versatile design flexibility, which facilitate the propagation of electromagnetic waves along the dielectric-metal interface. Owing to their ability to overcome the diffraction limit, SPPs have led to proposals for the manipulation and enhancement of surface waves using subwavelength devices [8,9]. The technology has shown vast potential for applications in areas such as polarization detection [10], biosensing [11,12], super-resolution imaging [13–15], high-density data storage [16,17], and other related fields. In the visible band, SPPs have been extensively utilized [18–20]. However, their binding ability diminishes significantly in the terahertz (THz) band, due to the metal's near-perfect conductivity. To mitigate this limitation and achieve robust confinements of microwaves and THz waves, a periodically folded metal structure has been proposed to support confined surface waves, referred to as spoof SPPs [21–23]. Although their generation mechanism is different from that of optical SPPs, spoof SPPs display similar features, including dispersion, subwavelength confinement, field enhancement, and sensitivity to the surrounding environment. Recent studies have indicated that the properties of spoof SPPs at THz frequencies—such as dispersion and subwavelength constraints—resemble those of visible light [24–26]. Several practical applications utilizing spoof SPPs have been proposed, driving the increasing demand for on-chip functional devices in THz systems. To enhance system integration, various THz on-chip devices, such as logic gates [27,28], refractive index gradient lenses [29], and demultiplexers [30], have been designed. However, those functional devices are far from sufficient for the development of the on-chip system. Ring resonators (RRs) are conventional optical devices that are widely utilized in silicon photonics for spectral filters [31–34], but they are used less in SPPs.

In this study, based on coupling theory and RRs theory [35], a band-stop filter and optical splitters are designed and verified through numerical simulation. The operating frequency of these devices is directly influenced by the radius of the RR and the separation between the straight waveguide and the resonator. By physically cascading RRs of varying radiuses, the band-stop filter's operating frequency can be broadened, thus expanding its bandwidth. The center frequency of the filter is 0.529 THz, with a bandwidth of 0.005 THz and a minimum stopband attenuation exceeding 28 dB. The coupling between the straight waveguide and the RR can be controlled by the gap width; thus, asymmetric RRs are adopted. In a single asymmetric RR rotational ADM, the spoof SPPs can be transmitted forward and backward by rotating the ring. In the case of two asymmetric RRs, the spoof SPPs can be transmitted along different ports. Thus, the optical shunt function is illustrated by considering two states of the unrotated and rotated RR structure, demonstrating its effective single-frequency division capability. This study expands the design possibilities for on-chip THz communication devices. It has a good single-frequency division function. It provides more possibilities for the design of on-chip THz communication devices.

2. Materials and Methods

As illustrated in Figure 1a, the spoof SPP device predominantly consists of a straight waveguide and a looped waveguide. Those waveguides are composed of the same metal pillars and arrayed on metallic surfaces. In front of the device, hole gratings are adopted to couple free-space THz radiation to surface waves. For operations in the THz frequency range, the parameters of periodic pillars in waveguides are chosen as a = 50 µm, b = 80 µm, h = 100 µm, and p = 100 µm, as shown in the inset of Figure 1a.

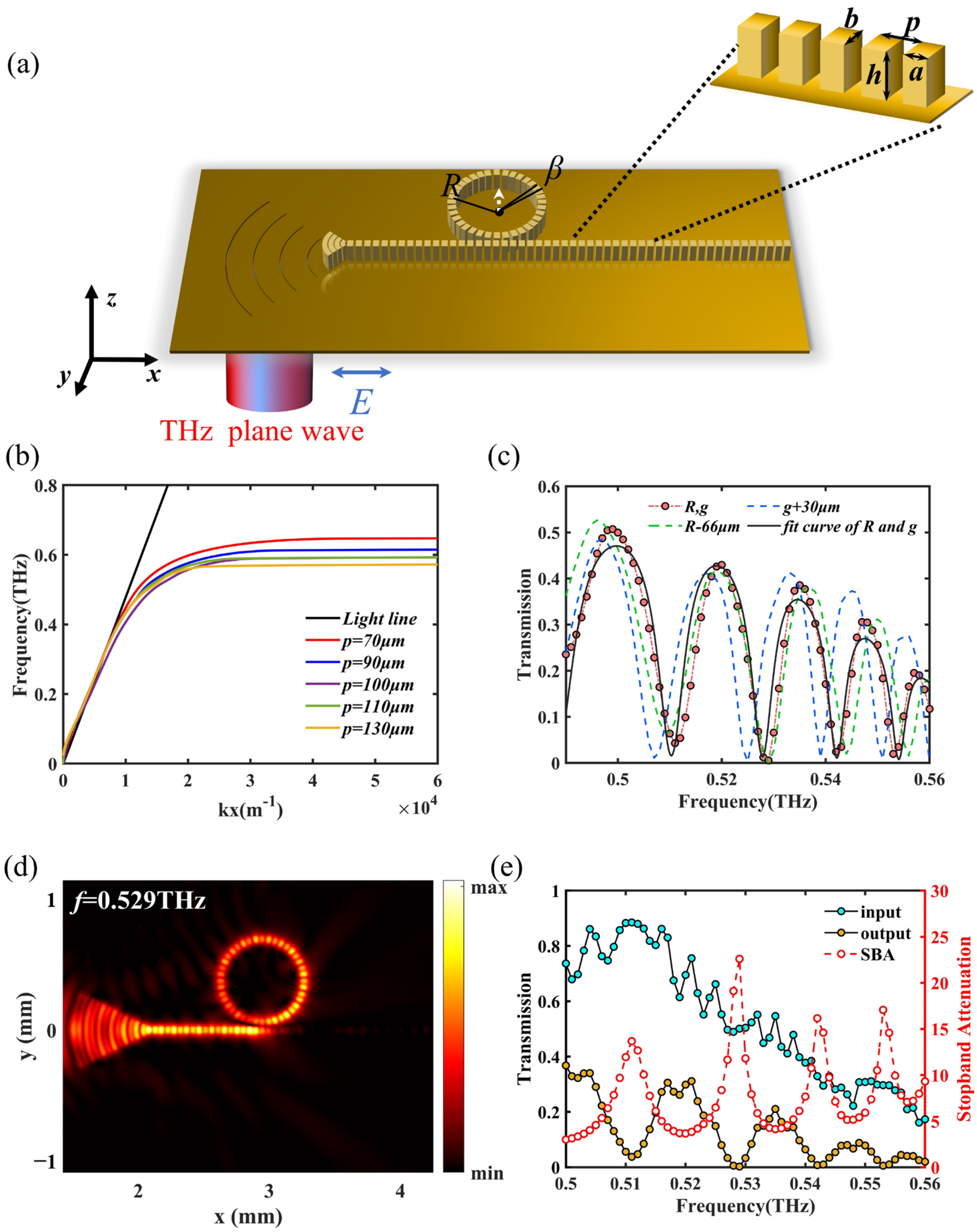

Figure 1. (**a**) Schematic of the device based on the RR, with geometrical parameters shown in the inset. (**b**) Dispersion relation of the spoof SPP modes for different periods p. (**c**) The normalized transmission spectra of an RR as a function of ring radius and gap width. Three sets of RR parameters: ring radius R = 700 μm and the gap width g = 40 μm, $R-66$ = 634 μm and g = 40 μm, and R = 700 μm and $g + 30$ = 70 μm. The black line is the fitting line. (**d**) The normalized simulated electric component $|E_z|$ distribution at 0.529 THz. (**e**) The normalized transmittance of ports and minimum attenuation in stopband (red wire).

The dispersion relation of the SPP mode in this structure is analyzed numerically by using the eigenmode solver of CST Microwave studio. In the simulation, both pillars and the substrate are treated as perfect conducts, the periodic boundary conditions are applied in the x-directions, and the phase variation in the x direction was φ. The eigenfrequency corresponding to each phase can be calculated to vary the phase from 0° to 180° with a step of 5°. The values of k_x were obtained based on the equation $k_x = \varphi\pi/180p$, where p is the period of the unit cell. The calculated dispersion curves are displayed in Figure 1b. The propagation constant k_x of the spoof SPP became larger than the light line (black line) with increasing frequency, which means that the textured surface with pillars exhibits significant field confinement ability. The effective refractive index of the spoof SPP modes can be calculated by $n_{eff} = k_x/k_0$.

The looped waveguide is the ring of radius R, which is positioned by the side of the straight waveguide. The $\beta = 6°$ is the angle of the two adjacent pillars, corresponding to the center of the circle. The pillars in the ring have the same geometric parameters as those in a straight waveguide except for the period p_r ($p_\mathrm{r} = \beta R\pi/180$). In general, after the surface waves couple to the ring and build up a round trip, the phase shift equals the integer times of 2π, the SPPs produce interference, and the resonance will occur. The resonance frequencies are defined as [36]:

$$f_\mathrm{res} = \frac{mc}{2\pi R n_{eff}}, m = 1, 2, 3 \ldots \tag{1}$$

The resonance frequencies are affected by the radius R and the effective refractive index n_{eff}. Previous studies have demonstrated that the geometric dimensions of the metal structure significantly impact the dispersion relation of the SPP mode [37]. In Figure 1b, the propagation constants of SPP modes for the different values of p_r, which varied from 70 to 130 μm, were displayed. The k_x becomes larger with increasing p_r at the same frequency. Hence, the effective refractive index can be regulated by changing the period of microstructure. Specifically, the propagation constants of the RR and the straight waveguide should be approximately equal, thereby reducing discrepancies in propagation constants and enhancing potential coupling effects.

The devices were designed and simulated using the time domain solver of CST (version 2020). A 5.2 × 10.4 mm^2-sized aluminum block with a 0.2 μm thickness is treated as the substrate. The boundary conditions in the x and y directions are set to open, and the boundary condition in the z direction is set to open (add space). On the metal film, an array of arc-shaped curved slits is employed to couple free-space THz radiation into surface waves. Each curved slit has a width of 40 μm, arranged at a period of 500 μm along the radial x direction, corresponding to excited SPPs at a frequency of 0.6 THz. A plane wave was used as the source to excite the SPPs. The first device was designed to have 700 μm-radius rings, separated by a 40 μm-gap (the minimum distance between the edge of the waveguide and the edge of the ring) from a straight waveguide. Based on Equation (1), the resonance should occur at 0.511 THz, 0.528 THz, 0.542 THz, and 0.553 THz within the range of 0.5 THz to 0.56 THz. The transmission spectra of the RR are periodic with respect to the phase accumulated by the ring per circulation, which is shown in Figure 1c. The resonant frequencies match the calculated results. The electric field $|E_z|$ distribution diagram at 0.529 THz is shown in Figure 1d, with a good filtering effect. The transmission ratio T is expressed as [33]:

$$T = \frac{P_\mathrm{out}}{P_\mathrm{in}} = L(\lambda) \times \frac{\alpha^2 + t^2 - 2t\alpha\cos\varphi}{1 + \alpha^2 t^2 - 2t\alpha\cos\varphi} \tag{2}$$

where P_out is output power, P_in is input power, $L(\lambda)$ is the total loss of the devices, α is the field attenuation factor per roundtrip in the ring, and t is the field transmission coefficient through the interaction region in the straight waveguide. The phase shift around the ring is given by $\varphi = 2\pi R(2\pi/\lambda)n_\mathrm{eff}(\lambda)$. When fitting the simulated data, the parameter was found to be at a = 0.55 and t = 0.6557 (black line in Figure 1c). Considering the influence of R and g on the resonance frequencies of the RR, the transmission spectra of the RR with different radii and the gap widths of RR are shown in Figure 1c. For the RR with a radius of 634 μm and a similar effective refractive index, the fitting parameters are $a \approx 0.58$ and

$t \approx 0.7$. It indicates that the field attenuation in the ring increases as the radius decreases. In addition, the gap width also has an impact on the transmission spectra. The transmission spectra for different gap widths are displayed in Figure 1c; as the gap width increases to 30 μm, the resonant frequency decreases as a whole due to the increase in optical path. In this case, the fitting parameter of $a \approx 0.55$ remains constant, and the transmission coefficient t increases to 0.72. It indicates that when the width gap is larger, there is a weaker coupling effect. Therefore, when the radius of the RR remains constant, altering the gap width of g allows for the precise control of the coupling effect. When the variation in g is sufficiently large, three coupling states can occur between the straight waveguide and the RR: under-coupled, over-coupled, and fully coupled. In both the under-coupled and over-coupled states, the resonant effect of the ring is suppressed. In the under-coupled state, increasing the coupling distance leads to a shift in the resonant frequency. In the over-coupled state, the coupling region is larger than the distance that is required for complete coupling corresponding, causing the wave to begin coupling back into the input waveguide. In the state of full coupling, the resonant function of the ring operates optimally. Determine the optimal coupling gap by evaluating the transmittance [31], as shown in Figure 2a. The bending radius of the curvature is R' = 930 μm, and the operating frequencies are 0.522 THz and 0.5315 THz. The $T = P_2/P_{in}$ is the transmission efficiency for the coupling between a curved waveguide and a straight waveguide, as presented. By analyzing different coupling gaps in Figure 2b, it is possible to estimate that the RR can achieve complete coupling with the straight waveguide at $g \approx 70$ μm.

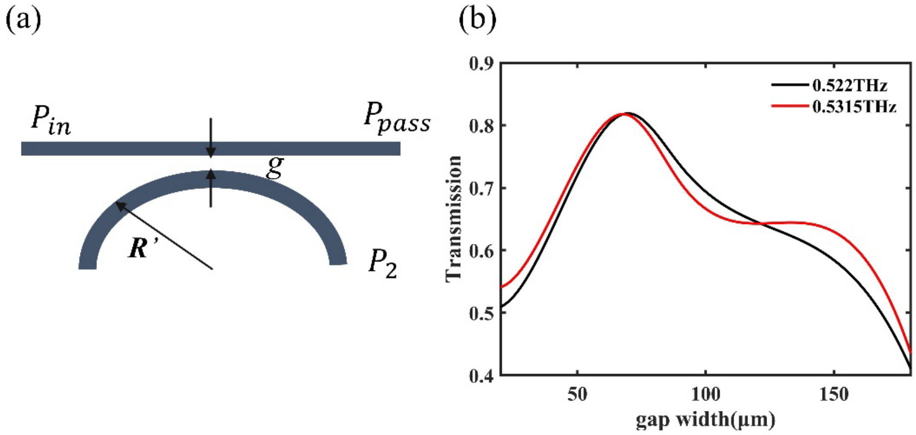

Figure 2. (**a**) Coupling between a curved waveguide and a straight waveguide. (**b**) Setting the RR's radius at R' = 930 μm. The transmittances of curved waveguide are affected by changes in g, at 0.522 THz and 0.5315 THz.

The stopband attenuation (*SBA*) and the quality factor (Q-factor) serve as crucial criteria for assessing the quality of resonant filtering. Within the stopband, a specific frequency point (or frequency range) is designated as the benchmark for evaluating the minimum suppression attenuation. To obtain this value, the ratio of the output power at this frequency point to the input power is calculated, and this ratio is expressed as [38]:

$$SBA = 10 \log_{10} \frac{|P_{\text{in}}|}{|P_{\text{out}}|} \tag{3}$$

At a center frequency of 0.528 THz, the device has a minimum stopband attenuation of 22 dB, as shown in Figure 1e. The quality factor (Q-factor) represents the number of oscillations before the energy decays to 1/e of the initial vale as [39]:

$$Q = \frac{\lambda}{\Delta\lambda_{FWHM}} \tag{4}$$

where ΔFWHM is the full width at the half maximum of a resonance peak. The Q-factor is about 180 at 0.528 THz for an RR structure, with a gap width of 40 μm and a radius of 700 μm. Compared to the filter device consisting of two identical split-ring structures (Q ≈ 50) [40] and the terahertz filters fabricated from graphene metamaterials (Q ≈ 140) [41], this designed RR demonstrates a superior Q-factor. Although this design can also achieve high-intensity filtering like devices based on the principle of plasmonically-induced interference [42,43], it exhibits a relatively lower transmission efficiency within the passband.

3. Results

3.1. Band-Stop Filter

We cascade two RRs with distinct radii to achieve a band-stop filter with a stronger filtering effect. As illustrated in Figure 3a, cascaded RRs with the radius of R_1 = 700 μm and R_2 = 634 μm are positioned on either side of the straight waveguide to avoid field interactions between the resonators.

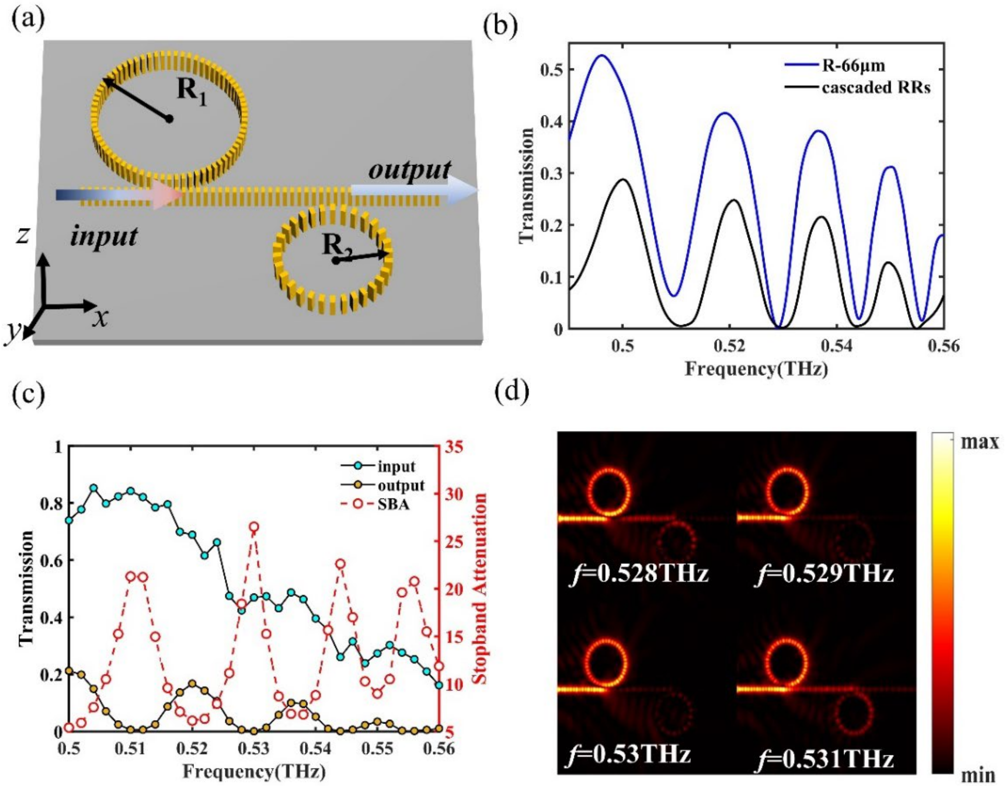

Figure 3. (**a**) Schematic of the band-stop filter with cascaded RRs. (**b**) Transmittance for a single RR with R = 634 μm and cascaded RRs with R_1 = 700 μm and R_2 = 634 μm, respectively. (**c**) The normalized port transmittance and stopband attenuation corresponding to frequencies. (**d**) The normalized simulated electric component $|E_z|$ distribution at different frequencies.

Despite the differing radius, these two RRs exhibit similar effective refractive indices, resulting in resonant frequencies that are closely matched. As illustrated in Figure 3b, the R_2 = 634 μm radius of a single RR operates at a frequency of 0.529 THz and has an operating bandwidth of 0.002 THz. The operating frequency of the cascaded stopband filter is the superposition of the resonant frequencies of two RRs of different radii; the stopband is widened to 0.005 THz. At the same time, due to the addition of an RR to stopband filters, the loss of the device will increase, resulting in a decrease in transmission efficiency. As illustrated in Figure 3c, within the resonance frequency range from 0.529 THz to 0.53 THz, the maximum stopband attenuation reaches 28 dB. Compared to the single RR filter shown in Figure 1e, the cascaded RR configuration achieves a 6 dB higher stopband attenuation, demonstrating a significantly stronger filtering effect. The electric field distributions $|E_z|$ at different frequencies are shown in Figure 3d. It gives the simulated electric field diagram at 0.528 to 0.531 THz. The filtering effect on the SPPs in this band is very significant. It can be used as a reference for widening the stopband filter device.

3.2. Add–Drop Multiplexer (ADM)

The implementation of an add–drop multiplexer (ADM) can be efficiently realized through the utilization of RRs. Figure 4a illustrates the diagram of the device, where an RR with a radius R_3 = 970 μm is placed in the middle of two straight waveguides. The gap width between RR and straight waveguides are g_1 = 65 μm and g_2 = 110 μm, respectively. The surface wave transmits from the input waveguide to the ring, where it couples to the second straight waveguide. At resonance, the incident field undergoes destructive interference at the pass port, causing the wave to be redirected to the drop port. According to the resonance condition defined in Equation (1), reverse output occurs at the resonance frequencies of 0.517 THz, 0.526 THz, and 0.541 THz. The transmission at the two output ports can be calculated as follows [44]:

$$T_{drop} = \frac{(1-t_1^2)(1-t_2^2)\alpha}{1-2t_1t_2\alpha cos\varphi + t_1^2t_2^2\alpha^2} \tag{5}$$

$$T_{pass} = \frac{{t_1}^2 - 2t_1t_2\alpha cos\varphi + \alpha^2 t_2^2}{1-2t_1t_2\alpha cos\varphi + t_1^2t_2^2\alpha^2} \tag{6}$$

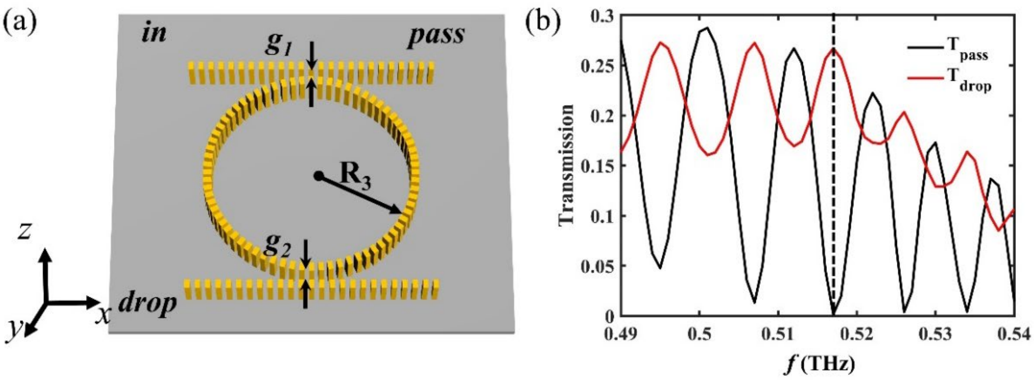

Figure 4. (**a**) Schematic diagram of the add–drop multiplexer. (**b**) The normalized transmittance of the pass port and the drop port.

The transmission for each port is calculated and depicted in Figure 4b. At an operating frequency of f = 0.517 THz, the power at the pass port is significantly lower than that at the drop port, which exhibits a transmission ratio of 170. This clearly demonstrates that the output strength at the drop port is positively correlated with the coupling coefficient. The coupling coefficient is highly sensitive to the gap spacing, decreasing exponentially as the gap width increases. To control the coupling efficiency and enable selective output port selection, the RR is designed with an asymmetric structure. The RR is divided into two parts along its diameter, as shown in Figure 5a. The upper and lower parts are composed of pillars with different widths b, which are 80 μm and 120 μm, respectively. The radius of the ring remains constant at R_3. The gap width between the RR and input waveguide is g_3 = 50 μm, and the gap width between the other waveguide is g_4 = 140 μm (θ = 0°). In this case, there is nearly full coupling between the input waveguide and RR, where the coupling effect between them is strong. The resonant function of RR is operating normally, as the transmission curve indicates by the solid line in Figure 5b. At the resonant with frequencies of 0.503 THz, 0.514 THz, 0.524 THz, and 0.5315 THz, the SPPs are outputs in the opposite direction along *output2*. As the RR rotates 180° around its center point of the inner diameter (θ = 180°), the gap widths change to g_3 = 10 µm and g_4 = 180 µm, causing the coupling effect between the input waveguide and the RR to shift into an over-coupled state. In this configuration, SPPs are coupled back into the input waveguide and propagate along the direction of *output1*. The transmittance of output port1 and port2 are displayed by the dashed lines in Figure 5b. Observing the change in the red line from solid to dashed, it can be inferred that the *output2* port transitions from open to closed as the rotation angle changes from 0° to 180°. At a frequency of 0.5315 THz, when the rotation state is 0°, RR directs the spoof SPPs to output port 2; when it is rotated to 180°, the RR redirects the spoof SPPs to the output1 port. The transmission values at output ports 1 and 2 are −5 dB and −9 dB, respectively. Figure 5c,d exhibit the electric field distributions at a specific frequency of f = 0.5315 THz for the RR oriented at 0° and 180°, respectively. Without rotation, the surface waves are directed through *output2*, whereas, after rotation, they are directed through *output1*. Based on this principle, selective forward and reverse SPP output can be achieved by controlling the rotation of the RR.

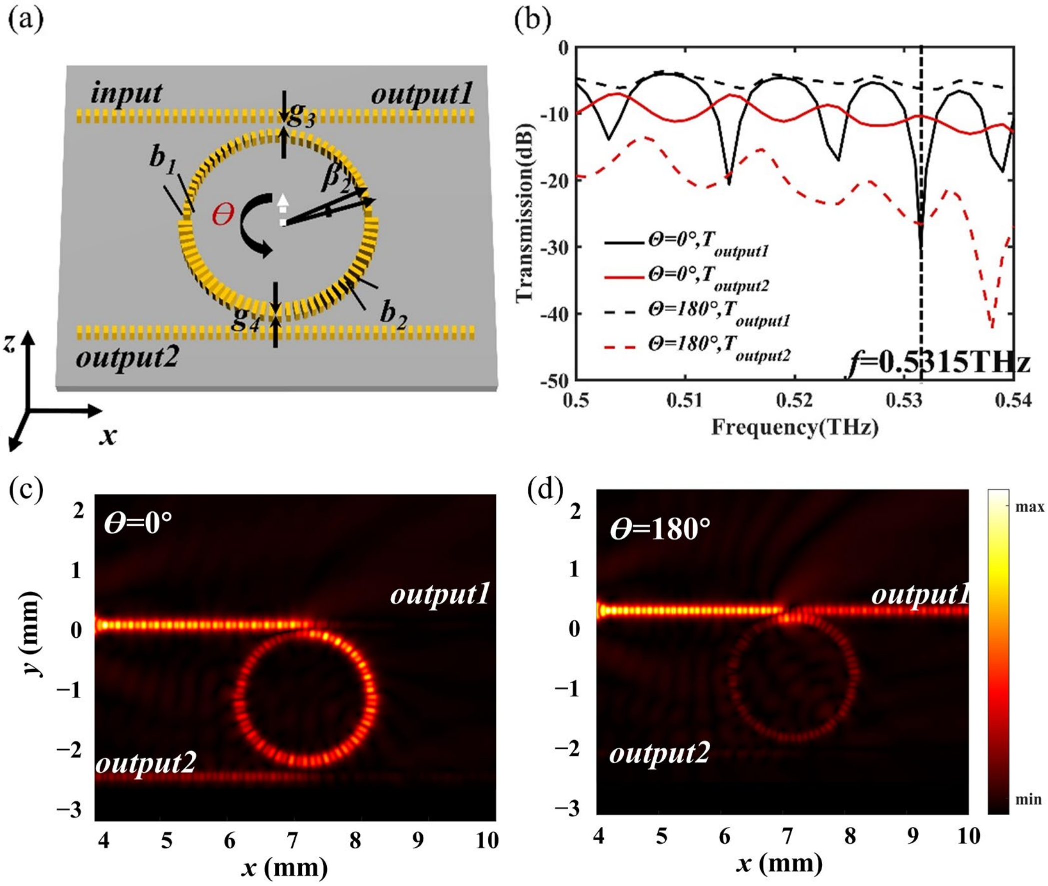

Figure 5. (**a**) Schematic diagram of add–drop multiplexer, with an asymmetric RR. (**b**) Comparison of the transmittance of *output1* and *output2* for ADM with different θ (**c**,**d**). The normalized simulated electric component $|Ez|$ distribution at 0.5315 THz for ADM with different θ of 0° and 180°, respectively.

Based on the above concept, another asymmetric ring is added and positioned side-by-side between the two straight waveguides. By controlling the coupling through the rotation of the RR in the same manner as before, SPPs can be selectively output through different ports. The structure and geometric parameters of the device are shown in Figure 6a. The pillars of different widths, b_1 = 80 μm and b_2 = 120 μm, remain unchanged. The radius of the ring remains the same as R_3. In this case, the gap width between the upper RR and the input waveguide is g_5 = 70 μm, the gap width between two RRs is g_6 = 80 μm, and the gap width between the lower RR and the other waveguide is g_7 = 85 μm (θ = 0°). Under the same curvature radius and spacing, the effective coupling length of a nonsymmetric coupler is larger than that of an asymmetric coupler by a factor of about $\sqrt{2}$ [45]. Therefore, the coupling states corresponding to these waveguides indicate that g_5 and g_7 correspond to fully coupled states, while g_6 corresponds to an under-coupled state. Due to the attenuation on the ring, the wave becomes weak after it propagates through the ring twice, and the second-order resonance can be ignored. The resonant frequency of the ring can be referenced based on the principles of a single ring, as depicted by the solid line in Figure 6b. The coupling between the RR and the input waveguide induces resonance effects at frequencies of 0.502 THz, 0.512 THz, 0.522 THz, and 0.53 THz. These frequencies also correspond to the resonant frequencies of the RR, with slight offsets due to different gap widths. At these frequencies, SPPs are transmitted from *output2*. After both RRs rotate by 180° around their center points of the inner diameter (θ = 180°), the gap widths change to g_5 = 30 μm, g_6 = 160 μm, and g_7 = 45 μm. For the RR with θ = 180°, a narrower gap width leads to the over-coupling effect between the input waveguide and the upper RR. Meanwhile, the wider gap between the two RRs leads to a weaker coupling effect, causing most of the SPPs at various frequencies to be coupled back into the input waveguide. These SPPs are then transmitted to the output. The transmissions at output ports 1 and 2 are −6 dB and −10 dB, respectively. Figure 6c,d exhibit the electric field distributions at a specific frequency f = 0.522 THz for the RRs oriented at 0° and 180°, respectively.

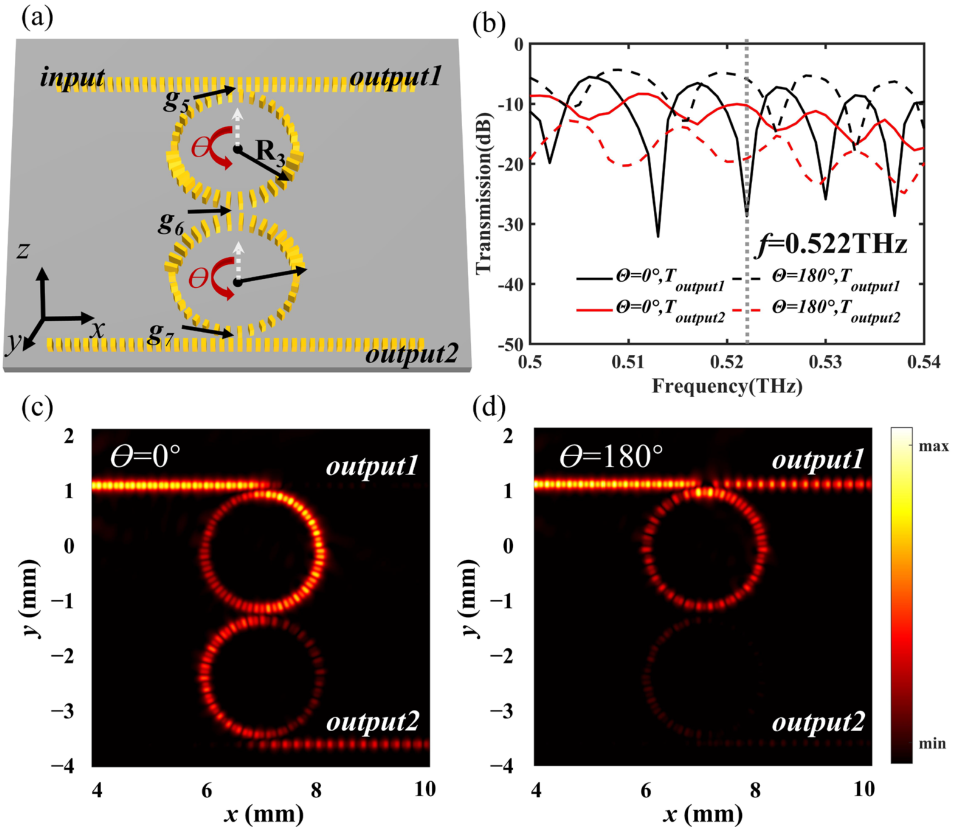

Figure 6. (**a**) Conceptual diagram and parameters of the add type coupled device. (**b**) The output loss of the port in the operating state of the device before and after rotation, respectively. (**c**,**d**) Normalized Ez electric field simulation before and after rotation, respectively, where z = 150 um.

Without rotation, the coupling between the straight waveguide and the RR is in the normal coupling state, with the output directed through *output2*. After rotation, the disconnection between the two RRs causes the spoof SPPs to be coupled back into the input waveguide, with the output now directed through output port 1. Based on this principle, the rotation of the RR controls the coupling, enabling selective outputs at different ports. Furthermore, the principle is straightforward, promoting the integration and miniaturization of on-chip THz systems.

4. Discussion

The technical application of RR plays a pivotal role in enabling large-capacity, high-speed integrated communication systems. In this study, the RRs are applied to control the propagation of spoof SPPs. A miniaturized and integrated band-stop filter and two types of splitters are designed and evaluated. The sensitivity of the RR's resonant wavelength to the resonator's radius is analyzed, and an expression relating the RR radius and central angle is provided for optimal design. Simulation data and theoretical calculations are fitted to validate the design's rationality. Building on this foundation, a cascaded RR band-stop filter and two dual-channel asymmetric rotating splitters are designed. These three functions are realized at operating frequencies of 0.529 THz, 0.5315 THz, and 0.522 THz, respectively. The cascaded RR band-stop filter exhibits a 0.005 THz wider bandwidth than the single RR filter, with a maximum stopband attenuation of 28 dB. In the single asymmetric RR rotational ADM (ADM), the transmissions at output ports 1 and 2 are -5 dB and -9 dB, respectively. When two asymmetric RRs are used, the transmissions at output ports 1 and 2 are -6 dB and -10 dB, respectively. This design and its simulation provide valuable insights for the design and optimization of coupling mechanisms between different waveguides. The cascaded RR band-stop filter and the asymmetric splitter serve as key components for the integration of terahertz on-chip systems, supporting further advancements in miniaturized and efficient terahertz communication technologies.

Author Contributions: C.L.: Formal analysis, model establishing and simulation, writing—original draft. S.G.: Simulation and discussion. M.S.: Data processing. Y.L.: Review and editing. Y.Z.: Writing—review and editing, conceptualization, and methodology. J.H.: Supervision. All authors have read and agreed to the published version of the manuscript.

Funding: The work is supported by National Natural Science Foundation of China (61905207, 61935015, and 62365018), Yunnan Fundamental Research Projects (202301AT070075), and Yunnan Expert workstation (202205AF150008).

Data Availability Statement: Data will be made available on request.

Conflicts of Interest: The authors declare that they have no known competing financial interests or personal relationships that could have appeared to influence the work reported in this paper.

References

1. Wu, J.; Nie, B.; Zhang, C.; Li, Y.; Gao, J.; Wang, X. Terahertz Non-destructive Imaging System Applied on Composite Materials Testing. In Proceedings of the 5th China and International Young Scientist Terahertz Conference, Chengdu, China, 22–24 March 2024; Chang, C., Zhang, Y., Zhao, Z., Zhu, Y., Eds.; Springer Nature: Singapore; Volume 2, pp. 56–60.
2. Fukasawa, R. Terahertz Imaging: Widespread Industrial Application in Non-Destructive Inspection and Chemical Analysis. *IEEE Trans. Terahertz Sci. Technol.* **2015**, *5*, 1121–1127.
3. Zhang, X.C. Terahertz wave imaging: Horizons and hurdles. *Phys. Med. Biol.* **2002**, *47*, 3667. [CrossRef] [PubMed]
4. Ellrich, F.; Bauer, M.; Schreiner, N.; Keil, A.; Pfeiffer, T.; Klier, J.; Weber, S.; Jonuscheit, J.; Friederich, F.; Molter, D. Terahertz Quality Inspection for Automotive and Aviation Industries. *J. Infrared Millim. Terahertz Waves* **2020**, *41*, 470–489. [CrossRef]
5. Tzydynzhapov, G.; Gusikhin, P.; Muravev, V.; Dremin, A.; Nefyodov, Y.; Kukushkin, I. New Real-Time Sub-Terahertz Security Body Scanner. *J. Infrared Millim. Terahertz Waves* **2020**, *41*, 632–641. [CrossRef]

6. Peng, Y.; Shi, C.; Wu, X.; Zhu, Y.; Zhuang, S. Terahertz Imaging and Spectroscopy in Cancer Diagnostics: A Technical Review. *BME Front.* **2020**, *2020*, 2547609. [CrossRef]
7. Chen, Z.; Han, C.; Yu, X.; Wang, G.; Yang, N.; Peng, M. Terahertz wireless communications. *China Commun.* **2021**, *18*, iii–vii. [CrossRef]
8. Han, Z.; Bozhevolnyi, S.I.; Bhushan, S.; Chauhan, V.S.; Easwaran, R.K. Radiation guiding with surface plasmon polaritons. *Rep. Prog. Phys.* **2012**, *76*, 016402. [CrossRef]
9. Ebbesen, T.W.; Genet, C.; Bozhevolnyi, S.I. Surface-plasmon circuitry. *Phys. Today* **2008**, *61*, 44–50. [CrossRef]
10. Jiang, Z.; Lu, J.; Fan, J.; Liang, J.; Zhang, M.; Su, H.; Zhang, L.; Liang, H. Polarization-Multiplexing Bessel Vortex Beams for Polarization Detection of Continuous Terahertz Waves. *Laser Photonics Rev.* **2023**, *17*, 2200484. [CrossRef]
11. Zhang, C.; Xue, T.; Zhang, J.; Liu, L.; Xie, J.; Wang, G.; Yao, J.; Zhu, W.; Ye, X. Terahertz Toroidal Metasurface Biosens. *Sensitive Distinct. Lung Cancer Cells* **2022**, *11*, 101–109. [CrossRef]
12. Zhang, Y.; Xia, Y.; Ling, H.; Zhang, J.; Li, K.; Yuan, C.; Ma, H.; Huang, W.; Wang, Q.; Su, X. Label-free diagnosis of ovarian cancer using spoof surface plasmon polariton resonant biosensor. *Sens. Actuators B Chem.* **2022**, *352*, 130996. [CrossRef]
13. Jepsen, P.U.; Cooke, D.G.; Koch, M. Terahertz spectroscopy and imaging—Modern techniques and applications. *Laser Photonics Rev.* **2011**, *5*, 124–166. [CrossRef]
14. Haxha, S.; AbdelMalek, F.; Ouerghi, F.; Charlton, M.D.B.; Aggoun, A.; Fang, X. Metamaterial Superlenses Operating at Visible Wavelength for Imaging Applications. *Sci. Rep.* **2018**, *8*, 16119. [CrossRef]
15. Zhang, X.; Liu, Z. Superlenses to overcome the diffraction limit. *Nat. Mater.* **2008**, *7*, 435–441. [CrossRef]
16. Zhang, S.; Chen, X.; Liu, K.; Li, H.; Lang, Y.; Han, J.; Wang, Q.; Lu, Y.; Dai, J.; Cao, T.; et al. Terahertz multi-level nonvolatile optically rewritable encryption memory based on chalcogenide phase-change materials. *iScience* **2022**, *25*, 104866. [CrossRef]
17. Bhushan, S.; Chauhan, V.S.; Easwaran, R.K. Ultracold Rydberg atoms for efficient storage of terahertz frequency signals using electromagnetically induced transparency. *Phys. Lett. A* **2018**, *382*, 3500–3504. [CrossRef]
18. Okamoto, H.; Onishi, S.; Kataoka, M.; Yamaguchi, K.; Haraguchi, M.; Okamoto, T. Characteristics of double-plasmonic-racetrack resonator to increase quality factor. *Opt. Rev.* **2013**, *20*, 26–30. [CrossRef]
19. Bozhevolnyi, S.I.; Volkov, V.S.; Devaux, E.; Laluet, J.-Y.; Ebbesen, T.W. Channel plasmon subwavelength waveguide components including interferometers and ring resonators. *Nature* **2006**, *440*, 508–511. [CrossRef]
20. Kryukov, A.E.; Kim, Y.K.; Ketterson, J.B. Surface plasmon scanning near-field optical microscopy. *J. Appl. Phys.* **1997**, *82*, 5411–5415. [CrossRef]
21. Kim, Y.K.; Lundquist, P.M.; Helfrich, J.A.; Mikrut, J.M.; Wong, G.K.; Auvil, P.R.; Ketterson, J.B. Scanning plasmon optical microscope. *Appl. Phys. Lett.* **1995**, *66*, 3407–3409. [CrossRef]
22. Li, Z.; Liu, L.; Xu, B.; Ning, P.; Chen, C.; Xu, J.; Chen, X.; Gu, C.; Qing, Q. High-Contrast Gratings based Spoof Surface Plasmons. *Sci. Rep.* **2016**, *6*, 21199. [CrossRef]
23. Pandey, S.S.; Gupta, B.; Nahata, A. Terahertz plasmonic waveguides created via 3D printing. *Opt. Express* **2013**, *21*, 24422–24430. [CrossRef] [PubMed]
24. Liu, L.; Li, Z.; Xu, B.; Gu, C.; Chen, X.; Sun, H.; Zhou, Y.; Qing, Q.; Shum, P.; Luo, Y. Ultra-Low-Loss High-Contrast Gratings Based Spoof Surface Plasmonic Waveguide. *IEEE Trans. Microw. Theory Tech.* **2017**, *65*, 2008–2018. [CrossRef]
25. Pendry, J.B.; Martín-Moreno, L.; Garcia-Vidal, F.J. Mimicking Surface Plasmons with Structured Surfaces. *Science* **2004**, *305*, 847–848. [CrossRef] [PubMed]
26. Zhang, Y.; Zhang, P.; Han, Z. One-Dimensional Spoof Surface Plasmon Structures for Planar Terahertz Photonic Integration. *J. Light. Technol.* **2015**, *33*, 3796–3800. [CrossRef]
27. Zhang, Y.; Xu, Y.; Tian, C.; Xu, Q.; Zhang, X.; Li, Y.; Zhang, X.; Han, J.; Zhang, W.; Yariv, A.; et al. Terahertz spoof surface-plasmon-polariton subwavelength waveguide. *Photonics Res.* **2018**, *6*, 18–23. [CrossRef]
28. Fu, Y.; Hu, X.; Lu, C.; Yue, S.; Yang, H.; Gong, Q. All-Optical Logic Gates Based on Nanoscale Plasmonic Slot Waveguides. *Nano Lett.* **2012**, *12*, 5784–5790. [CrossRef]
29. Zhang, Y.; Lu, Y.; Yuan, M.; Xu, Y.; Xu, Q.; Yang, Q.; Liu, Y.; Gu, J.; Li, Y.; Tian, Z.; et al. Rotated Pillars for Functional Integrated On-Chip Terahertz Spoof Surface-Plasmon-Polariton Devices. *Adv. Opt. Mater.* **2022**, *10*, 2102561. [CrossRef]
30. Gu, S.; Yuan, X.; Liu, L.; Sun, M.; Zhang, Y.; Xu, Q.; Han, J. Terahertz spoof surface plasmon polariton gradient index lens. *Results Phys.* **2023**, *47*, 106332. [CrossRef]
31. Ma, X.; Li, Y.; Xu, Q.; Han, J. Design of terahertz plasmonic wavelength division multiplexer assisted by whispering gallery mode resonators. *Opt. Quantum Electron.* **2023**, *55*, 927. [CrossRef]
32. Demirtzioglou, I.; Lacava, C.; Bottrill, K.R.H.; Thomson, D.J.; Reed, G.T.; Richardson, D.J.; Petropoulos, P.; Heebner, J.E.; Vincent, W.; Schweinsberg, A.; et al. Frequency comb generation in a silicon ring resonator modulator. *Opt. Express* **2018**, *26*, 790–796. [CrossRef] [PubMed]
33. Heebner, J.E.; Vincent, W.; Schweinsberg, A.; Boyd, R.W.; Jackson, D.J. Optical transmission characteristics of fiber ring resonators. *IEEE J. Quantum Electron.* **2004**, *40*, 726–730. [CrossRef]

34. Hou, L.; Tang, S.; Hou, B.; Marsh, J.H. Photonic integrated circuits for terahertz source generation. *IET Optoelectron.* **2020**, *14*, 136–142. [CrossRef]
35. Cheng, Q.; Kwon, J.; Glick, M.; Bahadori, M.; Carloni, L.P.; Bergman, K. Silicon Photonics Codesign for Deep Learning. *Proc. IEEE* **2020**, *108*, 1261–1282. [CrossRef]
36. Yariv, A.; Yeh, P.A. *Photonics: Optical Electronics in Modern Communications*; The Oxford Series in Electrical and Computer Engineering; Oxford University Press: Oxford, UK, 1997.
37. Bogaerts, W.; De Heyn, P.; Van Vaerenbergh, T.; De Vos, K.; Kumar Selvaraja, S.; Claes, T.; Dumon, P.; Bienstman, P.; Van Thourhout, D.; Baets, R. Silicon microring resonators. *Laser Photonics Rev.* **2012**, *6*, 47–73. [CrossRef]
38. Vaidyanathan, P.P. Chapter 5—Low-Noise and Low-Sensitivity Digital Filters. In *Handbook of Digital Signal Processing*; Elliott, D.F., Ed.; Academic Press: Cambridge, MA, USA, 1987; pp. 359–479.
39. Ou, X.; Yang, Y.; Sun, F.; Zhang, P.; Tang, B.; Li, B.; Liu, R.; Liu, D.; Li, Z. Wide-range, ultra-compact, and high-sensitivity ring resonator biochemical sensor with CMOS-compatible hybrid plasmonic waveguide. *Opt. Express* **2021**, *29*, 19058–19067. [CrossRef]
40. Fang, S.; Yang, Z.; Tao, Y.; Lv, W.; Jiang, J.; Zhang, D.-Q.; Wang, B.-X.; Yang, G.; Shu, F.-Z. Design and experimental realization of triple-band filtering metamaterial in sub-terahertz band enabled by conductivity coupling response of two identical split rings. *Opt. Laser Technol.* **2025**, *183*, 112345. [CrossRef]
41. Esfandiyari, M.; Lalbakhsh, A.; Jarchi, S.; Ghaffari-Miab, M.; Mahtaj, H.N.; Simorangkir, R.B.V.B. Tunable terahertz filter/antenna-sensor using graphene-based metamaterials. *Mater. Des.* **2022**, *220*, 110855. [CrossRef]
42. Li, H.-J.; Ren, Y.-Z.; Qin, M.; Wang, L.-L. Multispectral perfect absorbers using plasmonically induced interference. *J. Appl. Phys.* **2018**, *123*, 203102. [CrossRef]
43. Li, H.J.; Wang, L.L.; Zhai, X. Plasmonically Induced Absorption and Transparency Based on MIM Waveguides with Concentric Nanorings. *IEEE Photonics Technol. Lett.* **2016**, *28*, 1454–1457. [CrossRef]
44. Tan, Y.; Dai, D. Silicon microring resonators. *J. Opt.* **2018**, *20*, 054004. [CrossRef]
45. Yoneyama, T.; Tozawa, N.; Nishida, S. Coupling Characteristics of Nonradiative Dielectric Waveguides. *IEEE Trans. Microw. Theory Tech.* **1983**, *31*, 648–654. [CrossRef]